Journal of Colloid and Interface Science 576 (2020) 127–138

Contents lists available at ScienceDirect

Journal of Colloid and Interface Science

journal homepage: www.elsevier.com/locate/jcis

Evaporation of squeezed water droplets between two parallel hydrophobic/superhydrophobic surfaces

Xukun He [a], Jiangtao Cheng [a,*], C. Patrick Collier [b], Bernadeta R. Srijanto [b], Dayrl P. Briggs [b]

[a] Department of Mechanical Engineering, Virginia Tech, Blacksburg, VA 24061, USA
[b] Center for Nanophase Materials Sciences, Oak Ridge National Laboratory, Oak Ridge, TN 37831, USA

GRAPHICAL ABSTRACT

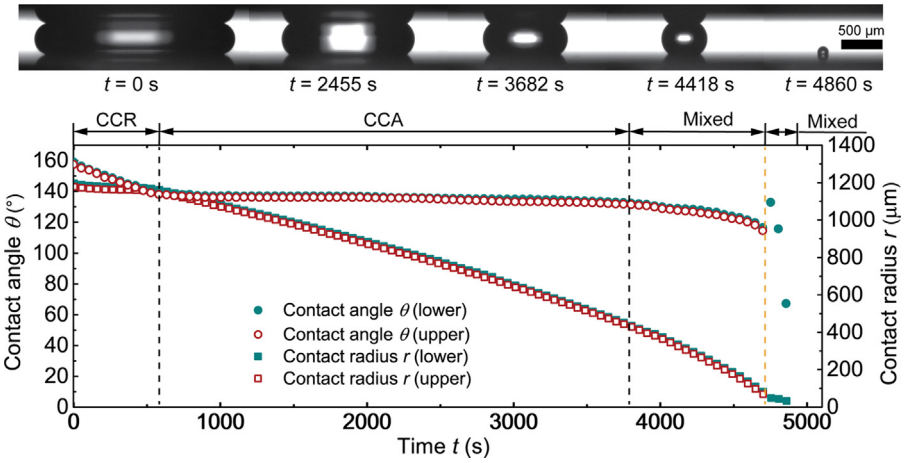

ARTICLE INFO

Article history:
Received 11 February 2020
Revised 1 May 2020
Accepted 1 May 2020
Available online 4 May 2020

Keywords:
Squeezed droplet evaporation
Confined space
Superhydrophobic
Diffusion-driven model

ABSTRACT

Hypothesis: A liquid droplet is apt to be deformed within a compact space in various applications. The morphological change of a droplet and vapor accumulation in the confined space between two parallel surfaces with different gaps and surface wettability are expected to significantly affect the evaporation dynamics of the squeezed droplet therein.
Experiments: Here the evaporation dynamics of a squeezed droplet between two parallel hydrophobic/-superhydrophobic surfaces are experimentally explored. By reducing the surface gap from 1000 μm to 400 μm, the evolution of contact angle, contact radius and volume of the evaporating droplet are measured. A diffusion-driven model based on a two-parameter ellipsoidal segment geometry is developed to predict the morphology and volume evolution of a squeezed droplet during evaporation.
Findings: Evaporation dynamics of a squeezed water droplet via the constant contact radius (CCR) mode, the constant contact angle (CCA) mode, or the mixed mode are experimentally observed. Confirmed by our ellipsoidal segment model, the evaporation of the squeezed droplet is significantly depressed with the decreasing surface gap, which is primarily attributed to vapor enrichment in a more confined geometry. A linear scaling law between droplet volume and evaporation time is unveiled, which is verified by a simplified cylindrical model.

* Corresponding author.
E-mail address: chengjt@vt.edu (J. Cheng).

https://doi.org/10.1016/j.jcis.2020.05.003
0021-9797/

Nomenclature

Latin

A (m^2)	the liquid-vapor interface area
a (m)	the length of the semi-major axis
b (m)	the length of the semi-minor axis
c (kg/m^3)	the mass concentration of water vapor
c_s (kg/m^3)	the mass concentration of vapor at the droplet-vapor interface
c_∞ (kg/m^3)	the mass concentration of ambient vapor at infinite distance from the droplet / the entrapped and enhanced vapor concentration
D (m^2/s)	the diffusion coefficient of water vapor in air
F (m^2)	the implicit function of contact radius r
h (m)	the height of squeezed droplet / the gap between two parallel surfaces
k (m^3/s)	the evaporation rate coefficient
n	the outward-pointing normal vector on the liquid–vapor interface
r (m)	the contact radius of squeezed droplet
r_u (m), r_l (m)	the contact radii of the squeezed droplet on upper and lower surfaces, respectively.
r_0^{CCA} (m)	the initial contact radius at the onset of CCA mode
R_{xy}(m), R_{xz} (m)	the curvature radii of the liquid–vapor interface in the x-y plane and the x-z plane, respectively.
RH_∞ (%)	the enhanced relative humidity in the confined space
t (s)	time
t_t (s)	the total time duration for the complete evaporation of the squeezed droplet
t_p (s)	the time when the evaporating droplet pinches off from the upper surface
t_0^{CCA} (s)	the onset of CCA mode during evaporation
t_{CCR} (s), t_{CCA} (s)	the time duration of CCR/CCA mode in the evaporation process of the squeezed droplet
$t^*, t^*_{CCR}, t^*_{CCA}$	the dimensionless time or time duration defined in the main text
V (m^3)	the volume of the evaporating squeezed droplet
V_0 (m^3)	the initial volume of droplet
$\dot{V}$ (m^3/s)	the volumetric evaporation rate
Bo	the dimensionless Bond number
Ca	the dimensionless Capillary number

Greek

α (m)	the geometry-dependent factor
λ (m^2/s)	the vapor concentration field dependent factor
θ_{CA}	the contact angle of a sessile droplet
μ (Pa · s)	the dynamic viscosity of water
θ	the contact angle of a squeezed droplet
ρ (kg/m^3)	the density of water
ε (m^2/s)	the evaporation coefficient in the power law of sessile droplet evaporation
γ (N/m)	the interfacial tension of droplet-vapor interface

Abbreviations

CCA	constant contact angle
CCR	constant contact radius
CVD	chemical vapor deposition
DI	deionized
RIE	reactive ion etching
SEM	scanning electron microscope

1. Introduction

The evaporation of a sessile liquid droplet on a solid surface has remained a very important topic of research in the past several decades because it plays a pivotal role in a variety of applications such as inkjet printing [1,2], micro- and nano-fabrications [3], cell/microparticle separation [4,5], spray cooling [6], chip cooling [7,8] and DNA mapping [9,10], etc. The evaporation of a sessile droplet is actually a challenging problem, and cannot be simply classified as a regular heat and mass transfer process because of its intricate involvement with fluid dynamics, fluid-solid interactions and contact line dynamics, i.e., a wetting phenomenon on surfaces with various physical (structural roughness) and chemical (wettability) properties [11,12]. In 1977, Picknett and Bexon first proposed a diffusion-driven evaporation model determining the evaporation rate of a sessile droplet by virtue of an analogy between the concentration field and the electric field [13]. In this seminal study, the researchers pointed out that the evaporation dynamics of a sessile droplet could be distinguished by three modes: (1) the constant contact radius (CCR) mode, in which the contact angle of the droplet decreases while the contact radius is kept as a constant; (2) the constant contact angle (CCA) mode, in which the contact line droplet keeps receding whereas the contact angle remains unchanged; and (3) the mixed mode, during which both the contact angle and the contact radius of the droplet vanish dramatically at the same time. And all the three modes have been experimentally observed on hydrophilic [14–17], hydrophobic [18–20] and superhydrophobic [21–24] surfaces. Since then, the evaporation dynamics of sessile droplets have been extensively studied by considering droplet evaporation from different aspects: (1) the effect of substrate properties including the thermal conductivity [25], temperature [23,26] and viscoelasticity [27] of the substrate and the wettability and topography of the solid surface; (2) the effect of the atmosphere including the room temperature, relative humidity and convection flow near the droplet [28–31]; and (3) the components of the droplet, such as the binary mixture droplet [32] or the droplet containing micro/nano-particles [33].

Nevertheless, much less attention has been paid to the evaporation of a droplet squeezed between two parallel surfaces and especially between two hydrophobic/superhydrophobic surfaces. In particular, vapor between the two substrates would be strongly concentrated at the vicinity of three-phase contact line, which may significantly hinder the evaporation of the squeezed droplet. In 2004, Leng experimentally observed the drying of organic droplets confined between two parallel hydrophilic plates from the bottom view [34], in which the slowing down of evaporation in the confined geometry was reported. In a series of subsequent studies [35–39] about the evaporation of squeezed colloidal droplets between two parallel glass substrates, the transport and deposition of colloidal particles due to the evaporation-induced flow were reported. However, in their experiments and theoretical analyses of evaporation, the wettability of glass substrates was not measured and the evolution of contact angle during evaporation was ignored. Besides, the few studies [40–42] about the evaporation of a pure fluid droplet between two hydrophilic surfaces mainly focused on the instability of the as-formed liquid bridge therein. To our knowledge, the only paper about the drying kinetics of an evaporating droplet between two hydrophobic plates was published very recently [43], in which the authors provided some detailed data about the evolution of contact angle and droplet volume during evaporation. However, the evaporation dynamics of the squeezed droplet in the confined space and how the

confinement suppresses the evaporation of the squeezed droplet are still unclear.

In this paper, the evaporation of a squeezed water droplet between two parallel hydrophobic/superhydrophobic surfaces was experimentally and theoretically investigated. First, the evaporation dynamics of a 2 μL water droplet between two parallel hydrophobic/superhydrophobic surfaces of 1000 μm apart was experimentally studied. The evaporation modes of a sessile droplet, i.e., CCA, CCR and the mixed mode, could be observed before the droplet pinched off the upper surface. Then the deposited droplet on the lower hydrophobic/superhydrophobic surfaces would behave as a sessile droplet that evaporated via the CCA, CCR and mixed modes, or directly evaporated in the mixed mode. Subsequently, the gap h between the two parallel surfaces was adjusted from 1000 μm to 400 μm to study the confined space effect on droplet evaporation. With decreasing gap h, the delayed onset of droplet pinch-off was observed and the whole evaporation time was found to be greatly prolonged. To elucidate suppressed droplet evaporation, we propose a diffusion-driven model by assuming the geometry of a squeezed droplet as an ellipsoidal segment. According to this model, the significant enrichment of vapor near the droplet, which is induced by the confined space, is found to be the dominant reason why a narrower gap h leads to the lower evaporation rate. Importantly, the evolvement of the contact radius r and the droplet volume during evaporation could be successfully predicted by this diffusion-driven model. Furthermore, a linear scaling law between droplet volume and evaporation time was realized based on our experimental results, which could be explained by a simplified cylindrical model compared to the more general ellipsoid segment model. This experimental and theoretical study on the evaporation dynamics of a squeezed droplet could deepen our understanding of this phase-change phenomenon in a confined geometry, and eventually offer us an effective approach to controlling droplet evaporation in various applications within a compact space including microfluidic systems [44], fuel cells [45] and electrowetting-based actuation systems [44,46].

2. Hydrophobic/Superhydrophobic surfaces preparation and experimental setup

Two kinds of hydrophobic or superhydrophobic surfaces were prepared for this study. To prepare a hydrophobic surface, we first spin coated a thin layer of fluoropolymer (PFC 1101 V, Cytonix Corporation) on a silicon wafer at 3000 rpm for 30 s, followed by wafer baking at 110 °C for 1 h. A water droplet on the fluoropolymer-coated surface has a contact angle of 118° as shown in Fig. 1(a), and its receding contact angle and advancing contact angle are 105° and 128°, respectively. To fabricate a superhydrophobic surface as shown in Fig. 1(b), a smooth silicon wafer was first etched by reactive ion etching (RIE) process (Oxford PlasmaLab 100 plasma dry etchers) [47] to form the nanofiber forest as shown in Fig. 1(c). Then the fluorinated silane (Trichloro(1H,1H,2H,2H-perfluorooctyl)-silane, Sigma-Aldrich) was conformally coated on the nanofibers through the standard chemical vapor deposition (CVD) process [48]. After baking at 110 °C for 30 min, as-formed nanostructured surface exhibits a contact angle of water as high as 158°, and the receding and advancing contact angles thereon are 152° and 166°, respectively. Considering the confined geometry effect, all the samples were cut into 2 cm × 2 cm pieces to preset the distance between the water droplet and the ambient (sample edges) for consistent evaporation studies.

Then thus-prepared two substrates with the same wettability were mounted in parallel onto two vertically adjustable linear-stages (Metric Z-Axis Stage, Edmund Corporation). A deionized (DI) water (Type I, >18 MΩ·cm resistivity) droplet of 2 ± 0.1 μL was generated by a syringe pump (EW-74905, Cole-Parmer Corporation) and deposited on the center of the bottom surface. The upper surface was lowered downward to squeeze the sessile droplet as illustrated in Fig. 2(a), and the gap h between the two surfaces was modulated by adjusting the height of the upper surface. The whole evaporation process of the squeezed droplet was recorded at 1.14 frame/s by a high-speed camera integrated on the contact angle measure system (Theta Lite, OneAttension Corporation). All experiments were conducted in a controlled laboratory environment with an ambient temperature of 21 ± 1 °C and a relative humidity (RH) of 35–40% and all cases were repeated for three times to verify the reproducibility of our experiments.

3. Theoretical analysis

Despite the complexity of the droplet evaporation process, we assume the evaporation of a squeezed droplet to be a quasi-stationary diffusion-driven process in an isothermal environment, and we ignore the effects of heat transfer, i.e., radiation, convection heat transfer with the atmosphere and heat conduction with the substrates. Therefore, this diffusion-driven model is dependent on the vapor concentration gradient across the liquid-vapor interface and the governing equation of droplet evaporation could be derived from Fick's second law as [13,14,49]:

$$\frac{\mathrm{d}V}{\mathrm{d}t} = -\frac{D}{\rho}\int \frac{\partial c}{\partial n}\mathrm{d}A \tag{1}$$

where V is the volume of the droplet, A is the liquid-vapor interface area, t is the evaporation time, ρ is the density of water, D is the diffusion coefficient of water vapor in air, n is the outward-pointing normal vector on the liquid-vapor interface and c is the mass concentration of water vapor surrounding the droplet. To solve the evaporation rate $\mathrm{d}V/\mathrm{d}t$ in Eq. (1), we need to choose the appropriate geometrical model for the squeezed shape of the droplet and to integrate the concentration gradient $\partial c/\partial n$ over the surface area A.

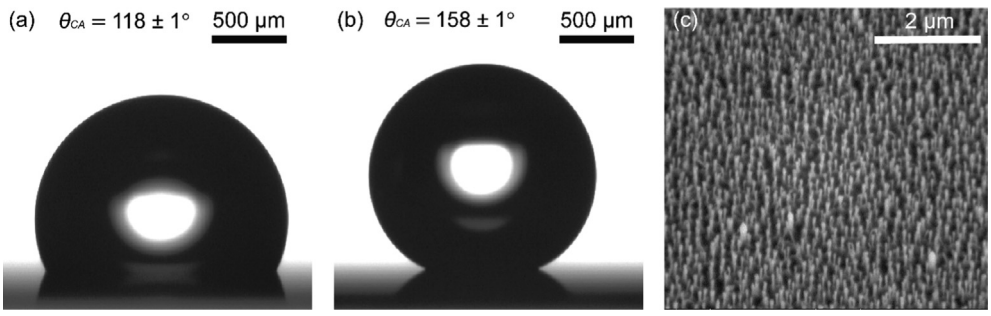

Fig. 1. Snapshots of a sessile water droplet on (a) a hydrophobic surface; (b) a superhydrophobic surface; and (c) SEM image of the black silicon nanofiber forest on the superhydrophobic surface.

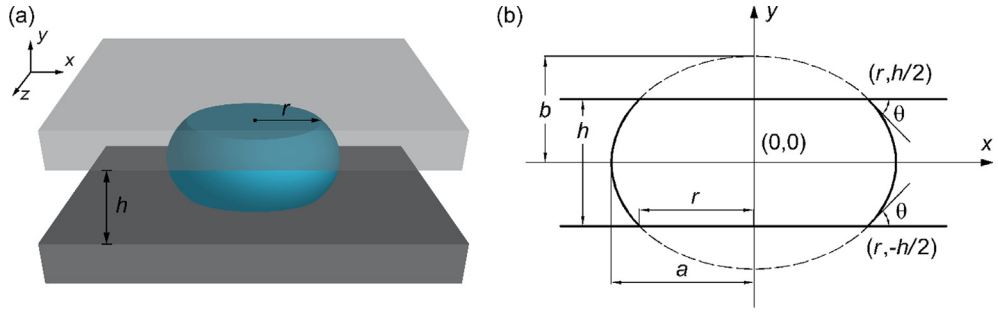

Fig. 2. (a) Schematic of a squeezed droplet confined between two parallel substrates (not in scale); (b) Diagram of the ellipsoid segment model of a squeezed droplet in the x-y plane.

3.1. Ellipsoidal segment model

For a sessile droplet sitting on a surface, two-parameter models, i.e., the classical spherical cap model [15], the ellipsoidal cap model [16] and the pseudo-spherical cap model [17] have been developed to study its evaporation dynamics. In these models, only two of the three parameters, i.e., contact radius r, contact angle θ and droplet height h, were used. For a squeezed droplet confined between two parallel surfaces, the height of the squeezed droplet is fixed by the gap h between the two surfaces, which means the traditional two-parameter models become unsuitable in this parallel-plate configuration. Therefore, in this work we choose the two-parameter ellipsoidal segment model by assuming the shape of the confined droplet as an ellipsoidal segment, which is the volume defined by cutting an ellipsoid with two parallel planes with gap h.

If the initial static contact angle θ of a water droplet on the two parallel surfaces is larger than 90° and the shape asymmetry induced by gravity is negligible, the profile of the ellipsoidal segment shape in x-y plane is analogues to an ellipse as illustrated in Fig. 2(b) and can be described by the following equation:

$$\frac{x^2}{a^2}+\frac{y^2}{b^2}=1 \tag{2}$$

where a and b are the lengths of the semi-major axis and the semi-minor axis, respectively. And based on the geometry relationship, the expression of a and b in terms of r, θ and h could be derived as:

$$a=\left(\frac{r(2r\tan\theta-h)}{2\tan\theta}\right)^{\frac{1}{2}},\quad b=\left(\frac{h(h-2r\tan\theta)}{4}\right)^{\frac{1}{2}} \tag{3}$$

The volume V and the surface area A, i.e., the liquid–vapor interface area, of the ellipsoidal segment could be calculated by rotating the elliptical segment ($-h/2 \le y \le h/2$) around the y axis:

$$V=\pi\int_{-h/2}^{h/2}x^2dy=\frac{\pi a^2}{b^2}\int_{-h/2}^{h/2}(b^2-y^2)dy=\pi hr\left(r-\frac{h}{3\tan\theta}\right) \tag{4}$$

$$A=2\pi\int_{-h/2}^{h/2}x\sqrt{1+\left(\frac{dx}{dy}\right)^2}dy$$
$$=\frac{2\pi a}{b^2}\int_{-h/2}^{h/2}\left[\left(b^4+\left(a^2-b^2\right)y^2\right]^{\frac{1}{2}}dy \tag{5}$$

Therefore, dA could be expressed as:

$$dA=\frac{2\pi a}{b^2}\left[\left(b^4+\left(a^2-b^2\right)y^2\right]^{\frac{1}{2}}dy \tag{6}$$

To solve the evaporation rate dV/dt in Eq. (1), we also need to know the vapor concentration gradient $\partial c/\partial n$ over the droplet surface, which has been proven to be dependent on the contact angle θ [50–52]. In this work, to simplify the integration, we took the same assumption as previous studies [16,17] that the concentration gradient over the surface area of a droplet is radially outward:

$$\frac{\partial c}{\partial n}=\frac{c_s-c_\infty}{2}\left(\frac{1}{R_{xy}}+\frac{1}{R_{xz}}\right) \tag{7}$$

where c_s is the mass concentration of vapor at the droplet-vapor interface, and c_∞ is conventionally taken to be the mass concentration of ambient vapor at an infinite distance from the droplet. However, in our system confined between two parallel plates, c_∞ would be more accurately represented by the entrapped (or enhanced) vapor concentration at the diffusion distance from the droplet, which is assumed to be a time-independent constant as discussed in Section 4.3. R_{xy} and R_{xz} are the two radii of curvature of the liquid–vapor interface in the x-y plane and the x-z plane, respectively, which could be calculated based on the ellipsoidal segment geometry:

$$\frac{1}{R_{xy}}=\frac{ab^4}{\left[\left(b^4+\left(a^2-b^2\right)y^2\right]^{\frac{3}{2}}},\quad \frac{1}{R_{xz}}=\frac{b^2}{a\left[\left(b^4+\left(a^2-b^2\right)y^2\right]^{\frac{1}{2}}} \tag{8}$$

By substituting Eqs. (6)-(8) into Eq. (1), the evaporation rate could be expressed as:

$$\frac{dV}{dt}=-\frac{\pi D(c_s-c_\infty)}{\rho}\left[h+a^2b^2\int_{-h/2}^{h/2}\frac{1}{b^4+\left(a^2-b^2\right)y^2}dy\right] \tag{9}$$

Here, to simplify the above formula, we define a vapor-concentration-field-dependent factor λ:

$$\lambda=\frac{2\pi D(c_s-c_\infty)}{\rho} \tag{10}$$

The integration of Eq. (9) could be performed according to the following three different cases, where the shape of a squeezed droplet would be assumed as a segment of (1) oblate spheroid if $a > b$; (2) prolate spheroid if $a < b$; and (3) sphere if $a = b$, respectively:

$$\frac{dV}{dt}=\begin{cases}-\frac{\lambda}{2}\left[h+\frac{2a^2b^2}{\sqrt{(a^2-b^2)b^4}}\tan^{-1}\left(\frac{h}{2}\sqrt{\frac{a^2-b^2}{b^4}}\right)\right] & \text{if } a>b\\ -\frac{\lambda}{2}\left[h+\frac{2a^2b^2}{\sqrt{(b^2-a^2)b^4}}tan^{-1}\left(\frac{h}{2}\sqrt{\frac{b^2-a^2}{b^4}}\right)\right] & \text{if } a<b\\ -\frac{\lambda h}{2}\left[1+\frac{a^2}{b^2}\right] & \text{if } a=b\end{cases} \tag{11}$$

To derive a simple diffusion-driven model, we assume the inverse tangent functions could be estimated by their small-value arguments:

$$\tan^{-1}\left(\frac{h}{2}\sqrt{\frac{a^2-b^2}{b^4}}\right) \approx \frac{h}{2}\sqrt{\frac{a^2-b^2}{b^4}},$$
$$\tan^{-1}\left(\frac{h}{2}\sqrt{\frac{b^2-a^2}{b^4}}\right) \approx \frac{h}{2}\sqrt{\frac{b^2-a^2}{b^4}} \quad (12)$$

Then Eq. (11) for the three different cases could be reduced to one simple equation:

$$\frac{dV}{dt} = -\frac{\lambda h}{2}\left[1+\frac{a^2}{b^2}\right] = -\frac{\lambda h}{2}\left[1-\frac{2r}{h\tan\theta}\right] \quad (13)$$

In Eq. (13), λ is a factor depending on the vapor concentration field between the droplet surface and the far field. The other component of Eq. (13) could be defined as a geometry-dependent factor α, whose effect could be regarded as the lumped effect of geometry changes, including the liquid–vapor surface area change and the surface curvature change during droplet evaporation:

$$\alpha = \frac{h}{2}\left[1-\frac{2r}{h\tan\theta}\right] \quad (14)$$

Based on the chain rule, the evaporation rate $dV(\theta,r)/dt$ in the CCA mode could be expressed as:

$$\frac{dV(\theta,r)}{dt} = \frac{\partial V}{\partial\theta}\frac{d\theta}{dt} + \frac{\partial V}{\partial r}\frac{dr}{dt} = \frac{dV}{dr}\frac{dr}{dt} \quad (15)$$

By differentiating Eq. (4), we obtain:

$$\frac{dV}{dr} = \pi h\left(2r - \frac{h}{3\tan\theta}\right) \quad (16)$$

Combining Eqs. (13), (15)–(16) together and separating the variables r and t to the two sides of the equation, we have:

$$-\frac{\lambda}{2}dt = \frac{M+Nr}{L+r}dr \quad (17)$$

where $M = \pi h^2/6$, $N = -\pi h\tan\theta$, $L = -h\tan\theta/2$ are the factors depending on the fixed surface gap h and the constant contact angle θ in the CCA mode.

By integrating Eq. (17) from t_0^{CCA} to t at the left-hand side and from r_0^{CCA} to r at the right-hand side, we have

$$F(r) = N\left(r-r_0^{CCA}\right) + (M-NL)\ln\left(\frac{L+r}{L+r_0^{CCA}}\right) = -\frac{\lambda}{2}\left(t-t_0^{CCA}\right) \quad (18)$$

where t_0^{CCA} is the onset of the CCA mode during evaporation, r_0^{CCA} is the corresponding contact radius at t_0^{CCA} and $F(r)$ is an implicit function of contact radius r. As indicated by Eq. (18), once h and θ are fixed,$F(r)$ in the CCA mode should follow a linear relationship with time t.

3.2. Cylindrical model

Obviously, the implicit function $F(r)$ of Eq. (18) is not mathematically "friendly". However, based on the following two approximations, i.e., a relatively lower contact angle ($\theta \to 90^\circ$) and a larger extent of squeeze ($h \ll r$), the ellipsoidal segment model could be simplified as a cylindrical model by approximating the significantly squeezed droplet as cylindrical shape:

$$\lim_{\substack{h\ll r,\\ \theta\to 90^\circ}} \frac{V}{r^2} = \lim_{\substack{h\ll r,\\ \theta\to 90^\circ}} \pi h\left(1-\frac{h}{3r\tan\theta}\right) \approx \pi h \quad (19)$$

$$V \approx \pi r^2 h \quad (20)$$

Here, the cylindrical approximation is assumed to be valid if $|h/3r\tan\theta| \le 0.1$, which means the ratio h/r of the surface gap over the contact radius needs to be lower than a critical value for certain contact angle, e.g., 1.70 for $\theta = 100^\circ$ and 0.25 for $\theta = 140^\circ$.

Therefore, the expression of evaporation rate dV/dt could be greatly simplified as:

$$\frac{dV}{dt} \approx -\frac{\lambda h}{2} \quad (21)$$

Based on the integration of Eq. (21), a scaling law between droplet volume V and time t could be expressed as:

$$V \sim V_0 - kt \quad (22)$$

where V_0 is the initial volume of droplet, k is the evaporation rate coefficient scaled as $k \sim \lambda h/2$. Because this cylindrical model ignores a portion of convex (or protruding) volume originated from the larger contact angle, it is not able to accurately predict the evaporation rate of a squeezed droplet for the cases with a larger surface gap h and a larger contact angle (i.e., between superhydrophobic surfaces). Moreover, this cylindrical approximation with a fixed surface gap h would gradually become invalid with the decreasing contact radius r during evaporation. Therefore, we use the scaling law of Eq. (22) to roughly represent the relationship between droplet volume V and time t during evaporation. Nevertheless, the linear scaling relationship resulting from the cylindrical model should still provide us some useful information for estimating the evolution of droplet volume with time.

4. Results and discussion

4.1. Evaporation dynamics of squeezed droplets

The representative snapshots of an evaporating droplet between two hydrophobic surfaces and two superhydrophobic surfaces with different surface gaps ($h = 400$ μm or $h = 1000$ μm) are shown in Fig. 3 respectively. All the snapshots were selected based on the nondimensional time $t^* = t/t_t$, where t_t is the total time for the complete evaporation of the squeezed droplet. As shown in Fig. 3, the evaporating droplets in the four cases followed a similar behavior: due to the constraint of the two surfaces, the volume reduction of the evaporating droplet gave rise to a continuous shrinkage of the contact line and finally evaporated as a sessile droplet after it pinched off from the upper surface. To quantitatively study the evaporation dynamics, the corresponding temporal evolution of contact angle θ and contact radius r of the evaporating droplets for the four cases are plotted in Fig. 4. The three traditional modes (CCR, CCA and the mixed mode) of sessile droplet evaporation could also be observed during the squeezed droplet evaporation. Here the three regimes of evaporation modes for the four cases were separately labelled in Figs. 4(a)-(d), in which the black dashed lines denote the transition time between different evaporation modes and the orange dashed lines indicate the onset moment t_p of the evaporating droplet pinching off from the upper surface.

As shown in Fig. 4, before and after the pinch-off time t_p, the evaporating droplets between two surfaces with different wettability and surface gaps followed essentially similar modes of evaporation dynamics. At the beginning of evaporation, the contact line of the droplet remained pinned while the contact angle continuously decreased, demonstrating the existence of the CCR mode during the evaporation dynamics of the squeezed droplet. Once the contact angle θ reduced to a certain value (~111° for hydrophobic cases and ~ 135° for superhydrophobic cases), the contact radius r began to shrink so that the CCA mode became dominant in evaporation. During the majority of the period, the evaporation dynamics of the droplet followed the CCA mode. And the contact angle θ and contact radius r on the upper surface were almost identical to those on the lower surface, indicating the up-down sym-

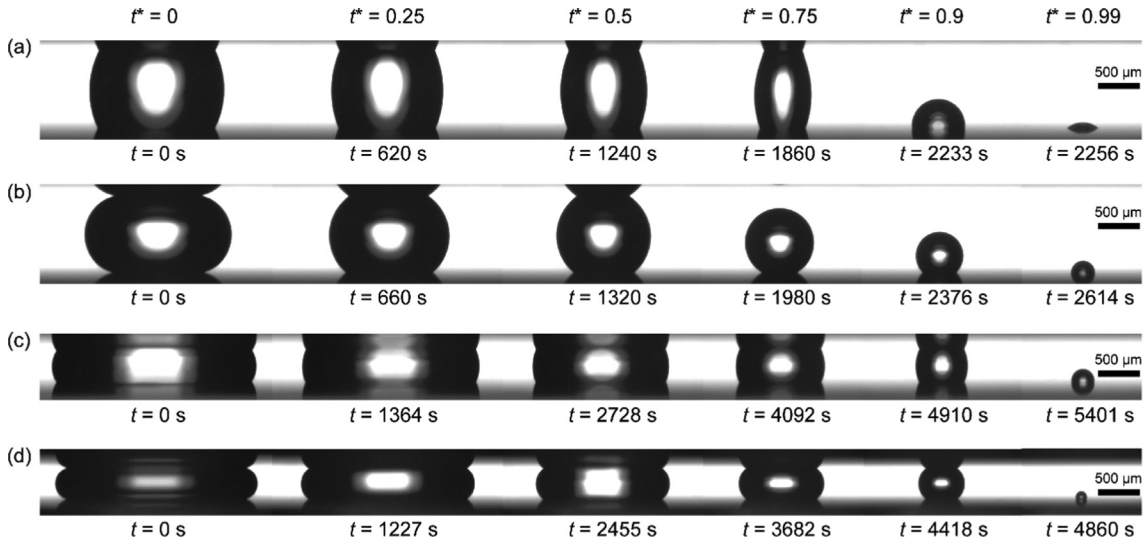

Fig. 3. Snapshots of droplet evaporation between two parallel (a) hydrophobic surfaces ($h = 1000$ μm); (b) superhydrophobic surfaces ($h = 1000$ μm); (c) hydrophobic surfaces ($h = 400$ μm); and (d) superhydrophobic surfaces ($h = 400$ μm). DI water droplet volume is 2 ± 0.1 μL in these experiments.

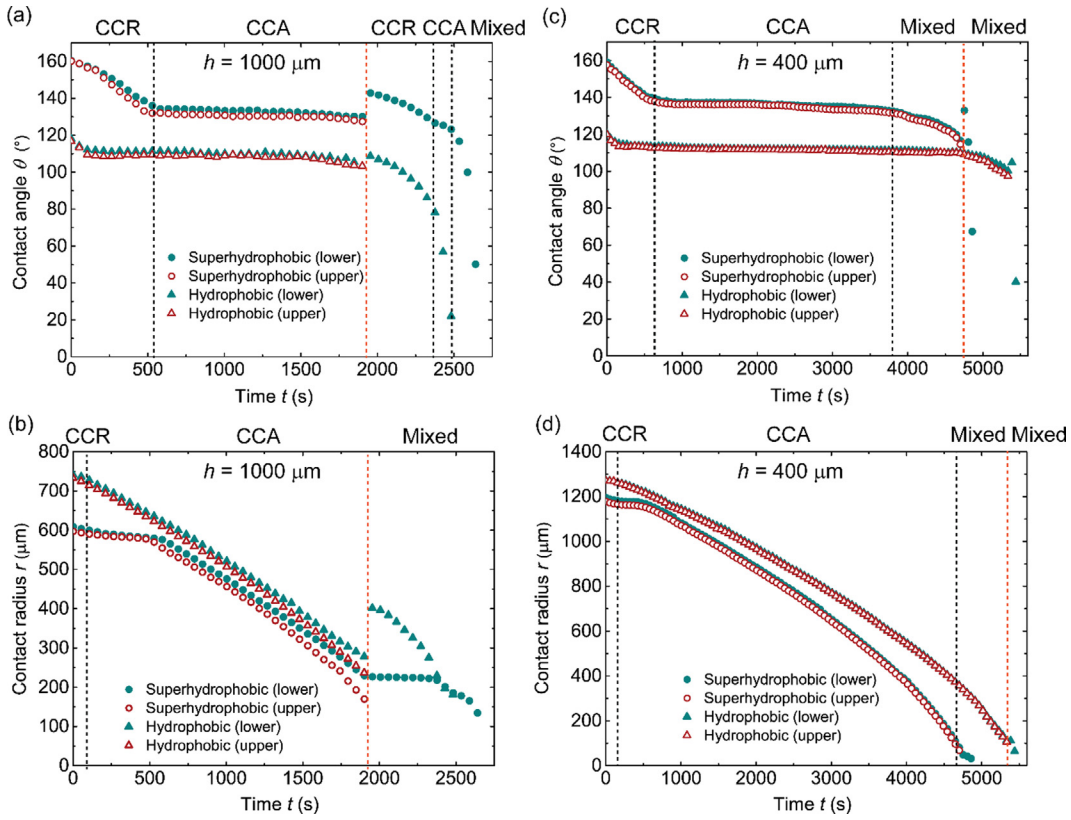

Fig. 4. (a) Temporal evolution of the contact angle θ of an evaporating droplet between two parallel surfaces with $h = 1000$ μm; (b) Temporal evolution of the contact radius r of an evaporating droplet between two parallel surfaces with $h = 1000$ μm; (c) Temporal evolution of the contact angle θ of an evaporating droplet between two parallel surfaces with $h = 400$ μm; and (d) Temporal evolution of the contact radius r of an evaporating droplet between two parallel surfaces with $h = 400$ μm. (The three regimes of evaporation dynamics for the four different cases are labeled in the four figures, respectively, as the following: superhydrophobic $h = 1000$ μm in Fig. 4(a), hydrophobic $h = 1000$ μm in Fig. 4(b), superhydrophobic $h = 400$ μm in Fig. 4(c), and hydrophobic $h = 400$ μm in Fig. 4(d).)

metric shape of the squeezed droplet due to the negligible effect of gravity.

Nevertheless, as the evaporation time t approached t_p, the shape symmetry was gradually broken with the increasing difference between the contact radius r_u on the upper surface and r_l on the lower surface until the evaporating droplet detached from the upper surface. It is noteworthy that only the CCR and CCA modes existed before t_p for the cases of the larger surface gap ($h = 1000$ μm). However, the mixed mode of evaporation, during which the contact line keeps retreating inward while the contact angle θ keeps decreasing, was observed near t_p in the two cases of narrower surface gap ($h = 400$ μm), which could be explained

by the significantly extended evaporation lifetime that will be discussed in Section 4.3.

With the rapid reduction of the liquid-solid contact area on the upper surface as shown in Figs. 4(b) and 4(d), the capillary force between the upper surface and the evaporating droplet was decreased. Once the force became too weak to overcome droplet gravity and the capillary force from the lower surface, the evaporating droplet would pinch off from the upper surface and deposit on the lower surface. The snapshots of the evaporating droplet before and after the pinch-off time t_p for the four cases are illustrated in Fig. 5. Two distinguished pinch-off behaviors of the evaporating droplet could be observed: (1) between the two hydrophobic surfaces, a small droplet remained on the upper surface after the breakup of the liquid bridge; and (2) between the two superhydrophobic surfaces, the evaporating droplet fully detached from the upper surface without leaving a small droplet on it. Similar stretching-induced breakup of a liquid bridge has been observed in some prior studies of droplet deposition on hydrophobic surfaces, in which the size of the resulting droplets was found to be strongly dependent on the retraction speed of needle or the upper surface during the contact-drop dispensing process [53–55]. In our work, the surface gap h was fixed during droplet evaporation, and hence the stretching of the evaporation droplet should be attributed to other reasons rather than the moving up of the upper surface. Indeed, whether an evaporating droplet between two surfaces is squeezed or stretched depends on whether the equivalent height h_s of the sessile droplet with identical volume is smaller than the surface gap h or not. In our experiments, the droplet was initially squeezed between two parallel plates and gradually became stretched once h_s got smaller than h due to the volume reduction of the evaporating droplet. Therefore, as the equivalent height h_s continued decreasing with time t approaching t_p, the evaporating droplet would behave like a prolate droplet stretched by the two substrates. On the other hand, the adhesion force on the superhydrophobic surface was so weak that the liquid bridge would eventually detach from the upper surface without leaving a smaller droplet.

Another non-negligible phenomenon during droplet evaporation is related to the contact angle hysteresis [56]. The evaporation of a droplet could be regarded as a dewetting process and the receding contact line in the CCA mode of evaporation indicates the measured contact angle during evaporation should be regarded as the receding contact angle rather than the static contact angle [57]. However, this statement deserves further reconsideration or revisiting on the structured superhydrophobic surfaces. In our experiments of squeezed droplet evaporation between two superhydrophobic surfaces, the evaporation-triggered wetting transition, e.g., the Cassie-to-Wenzel transition, might change the wetting state of the evaporating droplet and lead to an apparent reduction of contact angle [58–60], implying the measured contact angle during droplet evaporation could not be simply regarded as the receding contact angle on the superhydrophobic surfaces. Furthermore, the self-stretching phenomenon discussed above would also affect the measured contact angle, which could be demonstrated by the contact angle jumps before and after t_p as shown in Figs. 4(a) and 4(c).

After the evaporating droplet pinches off the upper surface and dwells on the lower surface, its evaporation dynamics should be similar with that of a sessile droplet. However, according to our experimental observations, the evaporation mode after pinch-off was jointly dependent upon the size of the deposited sessile droplet, surface wettability and the surface gap h. For the case of superhydrophobic surfaces with gap $h = 1000$ μm, we did observe that the evaporating droplet re-experienced the CCR, CCA and the mixed mode before the complete evaporation as shown in Figs. 4(a) and 4(b). For the other three cases, the droplet straightforwardly evaporated in the mixed mode to the end, which may be due to the narrower gap h or the relatively lower contact angle on the hydrophobic surfaces. On one hand, for the cases of $h = 400$ μm, the onset of pinch-off was significantly delayed and the volume of the deposited droplet on the lower surface was so small that it evaporated solely via the mixed mode, skipping the CCR and CCA modes. On the other hand, between hydrophobic surfaces, the contact angle of the small deposited droplet after t_p was about 100°, which may lead to the periods of both the CCR and CCA modes too short to be observed, as shown in Fig. 4(b).

4.2. Reconsideration of the effect of gravity on the evaporation dynamics of the squeezed droplet

The effects of gravity and viscous force on evaporation dynamics of microdroplets were usually ignored in most previous works [15–17,19]. In our work, the Capillary number ($Ca = \mu U/\gamma$, where μ is the dynamic viscosity of water, γ is the interfacial tension of droplet-vapor interface, U is the characteristic velocity) is used to evaluate the relative significance of viscous force and surface tension force. Although the characteristic velocity U inside the droplet could not be directly obtained in our experiments, it was believed to be very small ($< 10^{-5}$ m/s) in the diffusion-driven evaporation process according to several previous studies [61,62]. Therefore, Ca

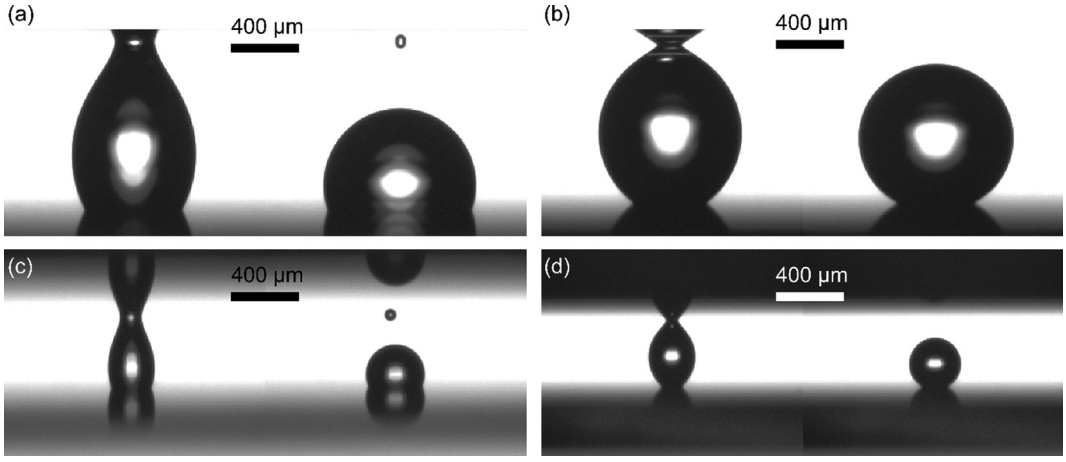

Fig. 5. Snapshots of an evaporating droplet before and after pinching off from the upper (a) hydrophobic surface ($h = 1000$ μm); (b) superhydrophobic surface ($h = 1000$ μm); (c) hydrophobic surface ($h = 400$ μm); and (d) superhydrophobic surface ($h = 400$ μm).

should be smaller than 1.4×10^{-7} in this work, which means the effect of viscous force could be ignored in comparison with the effect of surface tension force. And the Bond number ($Bo = \rho g h^2/\gamma$, where g is the gravitational acceleration) could be used to represent the relative importance of gravity and surface tension force, whose value is reduced from 0.134 to 0.022 due to the decreasing surface gap h from 1000 μm to 400 μm, also confirming the negligibility of gravity on the squeezed droplet evaporation. Moreover, the close overlap of both the contact radius curves and the contact angle curves of the upper and lower surfaces for each case as shown in Fig. 4 is also a strong validation of this assumption that the evaporation of a squeezed droplet could be regarded as up-down symmetric.

However, the evaporating droplet always tends to pinch off from the upper surface and deposits on the lower surface, implying that gravity does play a certain role in the pinch-off process. In fact, our experimental results do not contradict with our Bond number analyses. The whole experimental setup can be taken as a bistable system, in which depositing the droplet onto the upper surface or the lower surface are the two potential stable states. And the gravity, as the only source of asymmetric force acting on the evaporating droplet, could be regarded as an excessive load on the bistable system. During the whole evaporation process, the mismatch of contact radius ($|r_l - r_u|$) incurred by gravity would eventually lead to a remarkable asymmetry of the capillary forces with the two surfaces, resulting in the final deposition of the evaporating droplet on the lower surface. Therefore, the effect of gravity should be considered especially around the pinch-off time t_p. However, this pinch-off period with asymmetric contact radius and contact angle is very short compared with the whole evaporation period, which justifies the neglect of gravity in our theoretical analyses of squeezed droplet evaporation.

4.3. The effect of surface gap h on droplet evaporation in the confined space

With the decrease of surface gap h from 1000 μm to 400 μm, the total evaporation time t_t was increased by about 2.2 times between the hydrophobic surfaces (2481 s to 5456 s), and about 1.9 times between the superhydrophobic surfaces (2640 s to 4909 s), indicating that the total evaporation time could be significantly increased by decreasing gap h whereas the effect of hydrophobicity on the evaporation time could not be easily distinguished. Moreover, the delayed onset of pinch-off due to the narrower surface gap h contributed to the increased duration of the CCA mode, which is demonstrated by the increased dimensionless duration of the CCA mode $t^*_{CCA} = t_{CCA}/t_t = 0.53 - 0.67$ for the superhydrophobic cases and $t^*_{CCA} = 0.72 - 0.83$ for the hydrophobic cases. On the contrary, the very short duration of the CCR mode decreases slightly ($t^*_{CCR} = t_{CCR}/t_t = 0.18 - 0.14$ for the superhydrophobic cases and $t^*_{CCR} = 0.04 - 0.02$ for the hydrophobic cases), implying the dominant role of the CCA mode in the evaporation dynamics of the squeezed droplet. This is also the reason why we mainly apply our model to the CCA mode in the following section.

To quantitatively investigate the effect of surface gap h on the squeezed droplet evaporation, we applied our ellipsoidal segment model in Section 3.1 to our experimental data. First, we calculated the value of the implicit function $F(r)$, which is defined in Eq. (18), based on our measured contact radius r and contact angle θ. Here, the contact radius is the average value of contact radii on both the upper and the lower surfaces, and the constant contact angle is the average contact angle in the whole period of the CCA mode. In Fig. 6, we plot the implicit function $F(r)$ against evaporation time t during the CCA mode of the hydrophobic cases (Fig. 6a) and the superhydrophobic cases (Fig. 6b), respectively, with the surface gap h ranging from 400 μm to 1000 μm. Then a linear relationship is used to fit the data of $F(r)$ in the CCA mode for each case. As expected, the calculated $F(r)$ could be successfully regressed to a linear fitting curve as shown in Fig. 6, demonstrating the validity of our ellipsoidal segment model.

As indicated by Eq. (13), the evaporation rate dV/dt of the squeezed droplet is jointly determined by the vapor-concentration-field-dependent factor λ and the geometry-dependent factor α. Here, the temporal factor α could be calculated based on the real-time contact angle θ and contact radius r measured in the experiments. As shown in Fig. 7(a), the geometrical factor α increases with both the decreasing surface gap h and the enhanced surface hydrophobicity (from hydrophobic to superhydrophobic). However, this trend seemingly contradicts with our experimental observations, in which the completion of the evaporation process is significantly delayed between the two surfaces with a narrower gap h whereas the evaporation lifetime of the droplet between two superhydrophobic surfaces is only slightly different from that of the hydrophobic cases of same gap h. This fact indicates that the only possible reason for the suppressed droplet evaporation in the narrower space is due to the reduction of the vapor-dependent factor λ. According to Eq. (18), the value of λ could be easily obtained from the slope $-\lambda/2$ of the straight lines as shown in Fig. 6, and the calculated λ between both the superhydrophobic surfaces and the hydrophobic surfaces are plotted in Fig. 7(b) against the surface gap h. As expected, the factor λ increases with the increasing surface gap h but decreases with the enhancement

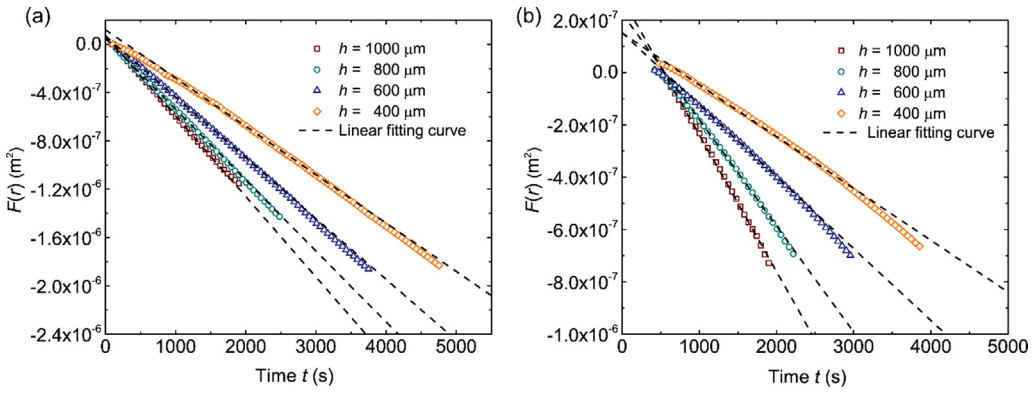

Fig. 6. Evolutions of the implicit function $F(r)$ calculated from Eq. (18) over time t for (a) the hydrophobic cases and (b) the superhydrophobic cases. (Only the calculated values of $F(r)$ in the CCA mode are shown.)

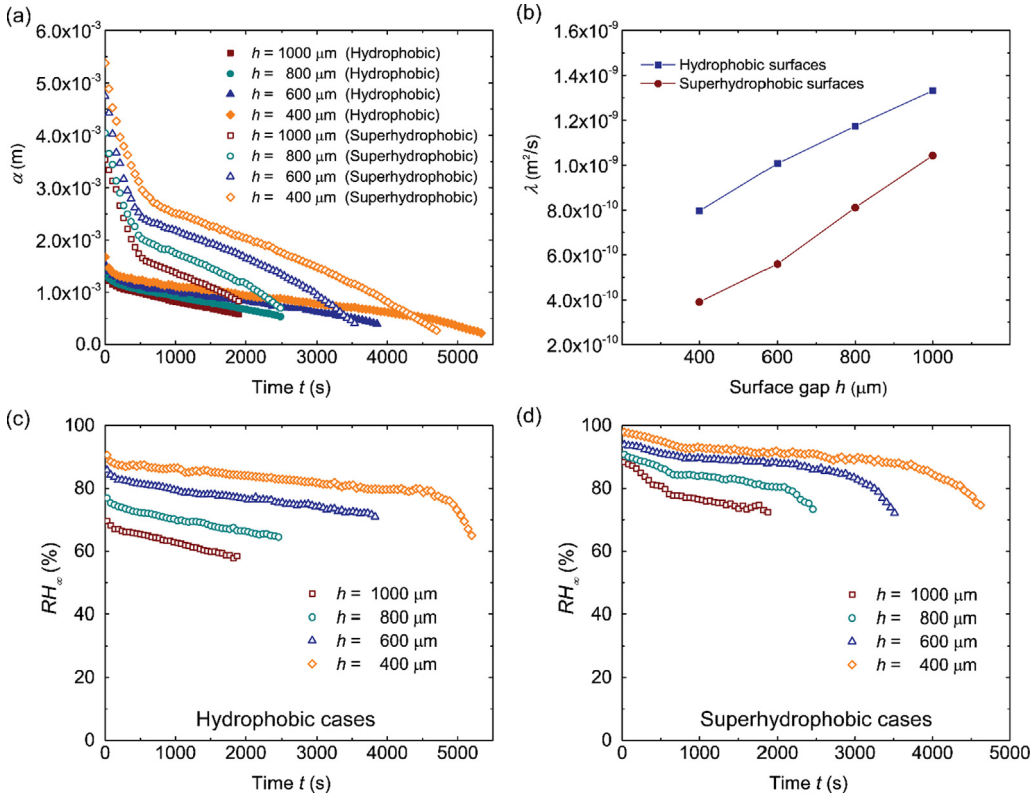

Fig. 7. (a) Temporal evolution of geometry-dependent factor α of an evaporating droplet between two parallel hydrophobic/superhydrophobic surfaces with various surface gap h; (b) Surface gap dependence of the vapor-concentration-field-dependent factor λ; (c) The temporal evolution of relative humidity RH_∞ between two parallel hydrophobic surfaces during evaporation; and (d) The temporal evolution of relative humidity RH_∞ between two parallel superhydrophobic surfaces during evaporation.

of hydrophobicity. Recall that λ as defined in Eq. (10) is a factor depending on liquid density ρ, vapor diffusion coefficient D, vapor concentration on the droplet surface c_s, and vapor concentration in the far field c_∞ in a combined manner. In our experiments with steady temperature and pressure, ρ, D and c_s could be regarded as constants, implying the increase of c_∞ due to the confined space is the only reason why λ decreases with decreasing h as shown in Fig. 7(b).

Regarding the evaporation of a sessile droplet in an open environment, the value of c_∞ can be always assumed as the ambient vapor concentration. However, the confined space in the parallel-plate configuration would induce the accumulation of vapor surrounding the evaporating droplet, thus the increased confinement in the narrower gap h finally gives rise to the higher value of c_∞. Moreover, the relatively larger contact angle on the superhydrophobic surfaces indicates a narrower wedge region formed between the solid surface and the droplet periphery near the three-phase contact line, which could entrap evaporated vapor in the vicinity of the contact line, leading to a lower λ between the superhydrophobic surfaces as well. And this is the reason why we define c_∞ as the entrapped (or enhanced) vapor concentration at the diffusion distance from the droplet surface in Section 3.1.

In order to verify the enhanced vapor concentration in the confined space between parallel plates, the relative humidity RH_∞ therein can be estimated by combining Eq. (10) and Eqs. (13)–(14) as:

$$RH_\infty = \frac{c_\infty}{c_s} = 1 - \frac{\rho\alpha\dot{V}}{2\pi D c_s} \tag{23}$$

where $\dot{V}$ is the volumetric evaporation rate of the droplet and could be estimated based on the temporal evolution of the droplet volume. The diffusion coefficient D of water molecules in air is taken as a constant value of 0.244 cm^2/s [63] and the saturated vapor concentration c_s at the room temperature is taken as 18.3 g/m^3 [64]. Here the temporal evolutions of the enhanced relative humidity RH_∞ between two parallel hydrophobic/superhydrophobic surfaces during evaporation are shown in Fig. 7(c) and (d), respectively. It is evident that the values of RH_∞ for all the eights cases are larger than the ambient relative humidity (35–40%) in our experiments. And the increasing RH_∞ with narrowing surface gap h also confirms our prediction of the enhanced vapor concentration in the confined space. For the cases with the same surface gap h but with different surface wettability, the vapor concentration between the superhydrophobic surfaces is larger than that between the hydrophobic surfaces, which is consistent with the decreasing trend of RH_∞ when the droplet evaporation changes from the CCR mode to the CCA mode. And the decreasing RH_∞ associated with a smaller contact angle could be explained by the lower extent of vapor enrichment in the wider wedge region, which is formed at the three-phase (solid-liquid-vapor) contact zone as mentioned above. In addition, although RH_∞ gradually decreases during droplet evaporation, the decreased level of RH_∞ is not very large, especially in the CCA mode (e.g., $RH_\infty = 67\% - 58\%$ for the hydrophobic case of $h = 1000$ μm; $RH_\infty = 93\% - 85\%$ for the superhydrophobic case of $h = 400$ μm). Therefore, it is reasonable to assume the corresponding entrapped vapor concentration c_∞ as a time-independent constant especially in our analysis of the CCA mode. In fact, the effect of vapor enrichment has been experimentally observed by Basu's group when they studied the sessile droplet evaporation dynamics in a confined channel [29–31]. The evaporation process of a confined sessile droplet therein was also found to be mitigated by the relative higher concentration c_∞ (i.e., larger than the ambient vapor concentration) induced by the confined

space. Furthermore, the researchers found that the value of c_∞ (c'_∞ in [29]) remains temporally constant during the droplet evaporation in the longer channels [29], which also confirms the validity of our assumption that c_∞ is a time-independent constant in Section 3.1 since the dimension of our substrate (~2 cm) is greatly larger than the squeezed droplet radius (~1 mm).

In summary, when a squeezed droplet evaporates in a confined space, the increase of the geometrical factor α would speed up the evaporation process whereas the decreasing vapor-dependent factor λ would slow down the evaporation, implying the enhanced vapor confinement due to the narrower surface gap h is the origin of the suppression of droplet evaporation within two parallel surfaces. Regarding these two factors, α could not be tuned if the droplet volume, surface wettability and surface gap h are fixed. However, the vapor-dependent factor λ is adjustable during evaporation if the vapor concentration can be modulated within the confined space. Therefore, the evaporation process of a squeezed droplet in a compact space could be greatly facilitated if the vapor surrounding the droplet is evacuated in a fast fashion. Besides, the competition between the vapor-dependent factor λ and the geometry-dependent factor α for cases with different hydrophobicity, i.e., the larger value of α and the smaller value of λ in the superhydrophobic cases versus the smaller value of α and the larger value of λ in the hydrophobic cases as shown in Fig. 7, could be used to explain why it is hard to differentiate the effects of different surface hydrophobicity on the evaporation process of a squeezed droplet.

4.4. Evaporation rate

By substituting the derived value of λ into Eq. (17), the theoretical value of contact radius in the CCA mode could be obtained by solving this implicit equation numerically. Fig. 8 displays the evolutions of both the theoretically predicted and the experimental values of contact radius r of the evaporating squeezed droplets between the two parallel hydrophobic/superhydrophobic surfaces with four different surface gaps h ranging from 400 μm to 1000 μm, respectively. Note that the experimental contact radius herein is also the averaged value of the contact radii on the lower and upper surfaces and we only plot the data before the pinch-off time t_p to verify our ellipsoidal segment model. Based on the theoretical values of contact radius, the theoretical volume changes of evaporating squeezed droplets between two parallel hydrophobic/superhydrophobic surfaces with four different surface gaps h could be predicted according to Eq. (4), which are plotted along with the experimental volume changes in Fig. 9, respectively. As indicated in Figs. 8 and 9, the excellent agreement between the experimental data and the theoretical models validates the ellipsoidal segment model as a useful predictor for the evolutions of contact radius and droplet volume. For the superhydrophobic cases with narrower surface gaps ($h = 400$ μm, 600 μm), our ellipsoidal segment model would underestimate the reductions of both the contact radius r and volume V when approaching t_p as shown in Figs. 8(b) and 9(b). And this underestimation could be ascribed to the reduced contact angle in the mixed mode and the increased asymmetry of contact radius near t_p as we discussed in previous sections.

Another important aspect of droplet evaporation is the scaling relationship between the droplet volume V and the evaporation time t. Regarding the evaporation of a sessile droplet, the power law of $V^{2/3} \sim V_0^{2/3} - \varepsilon t$ has been reported in previous studies [23,65], in which the value of the evaporation coefficient ε was found to be increased after the droplet evaporation transited from the CCR mode to the CCA mode. Similarly, the slope change of each V-t curve in Fig. 9 implies that the evaporation rate $\mathrm{d}V/\mathrm{d}t$ of the squeezed droplet between two parallel surfaces is also influenced by the evaporation modes of the droplet. However, there are two distinguishing features for the squeezed droplet evaporation. First, the volume evolution of the squeezed droplet follows a nearly linear relationship with time, i.e., $V \sim t$, rather than the conventional power law of $V^{2/3} \sim t$. This linear scaling relationship is consistent with our cylindrical model (Eq. (22)) in that the squeezed droplet could be approximated as a cylindrical droplet once the extent of squeeze is significant enough ($h \ll r$), or the contact angle of the evaporating droplet approaches 90° on the surfaces. As indicated by the scaling of coefficient $k \sim \lambda h/2$, the decreasing slope of the V-t curves with narrowing gap h as shown in Fig. 9 could be accounted for by both the lower h and the confinement-induced lower λ. Second, the evaporation rate in the CCA mode is larger than that in the CCR mode, which is contrary to the findings for the sessile droplet evaporation. This improvement of evaporation rate during the transition from the CCR mode to the CCA mode could be ascribed to the decreasing RH_∞ inside the confined space as shown in Fig. 7(c) and (d). Moreover, the receding contact line in the CCR mode might consecutively refresh the local concentration field of vapor near the contact line, which may moderate the effect of vapor enrichment between the substrates. With time t approaching the pitch-off time t_p, the remarkably shrunk contact radius r indicates that the assumption of $h \ll r$ does not hold anymore, which also accounts for the increasing deviation between the experimental data and the linear fitting curve near t_p.

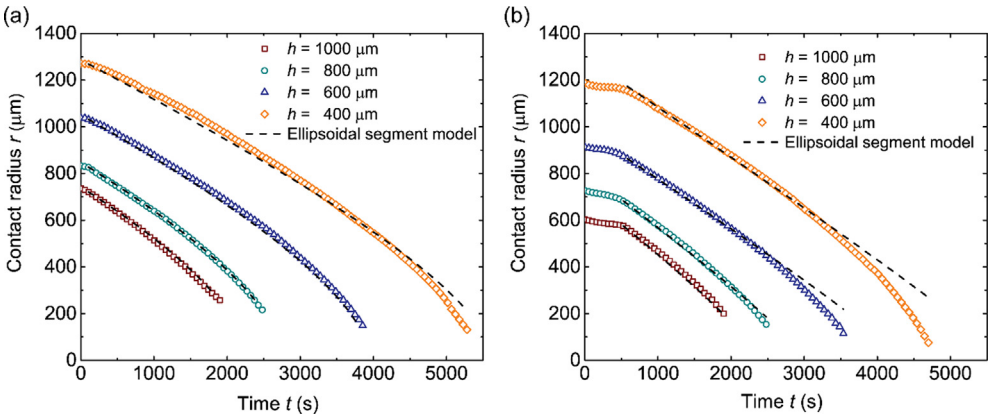

Fig. 8. Evolutions of the contact radius$r$ of an evaporating droplet over time t in the (a) hydrophobic parallel-plate cases and (b) superhydrophobic parallel-plate cases before the pinch-off time t_p (scatter circle: the experimental data; the dashed curve: theoretical value predicted by the ellipsoidal segment model).

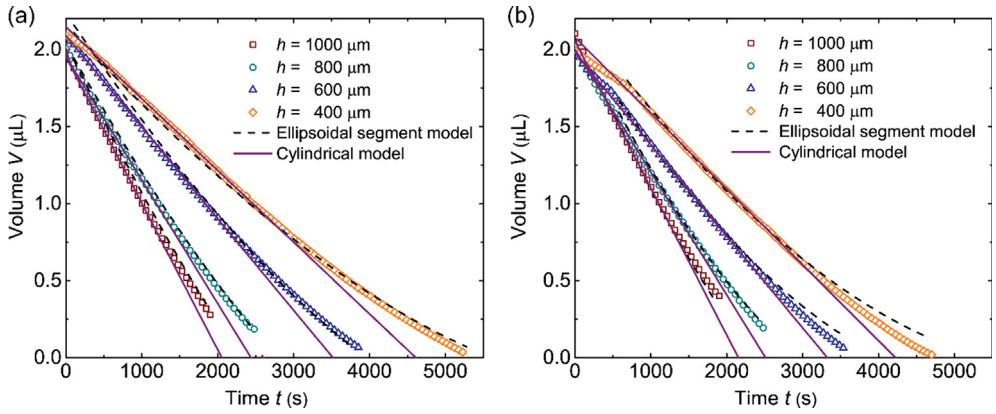

Fig. 9. Temporal evolutions of the volume of an evaporating droplet for (a) hydrophobic parallel-plate cases and (b) superhydrophobic parallel-plate cases before the pinch-off time t_p (scatter: experimental data; the black dashed curve: the values predicted by the ellipsoidal segment model; the purple dashed curve: linear fitting curve based on the cylindrical model.) (For interpretation of the references to colour in this figure legend, the reader is referred to the web version of this article.)

5. Conclusion

In this work, the evaporation dynamics of a squeezed water droplet between two parallel hydrophobic/superhydrophobic surfaces have been experimentally and theoretically investigated. In comparison to most previous studies of confined droplet evaporation, which mainly focused on either colloid particle transport inside the evaporating droplet while ignoring the contact angle change of droplet [34–36,38,39] or the liquid bridge instability between two hydrophilic surfaces during the evaporation [40–42], here we conducted the first systematic study on the evaporation dynamics of a squeezed water droplet between two hydrophobic/superhydrophobic surfaces by taking the effects of the confined space and the morphological (contact angle/contact radius of an evaporating droplet) change in to account.

A series of droplet evaporation experiments with a variety of surface gaps and surface wettability, i.e., hydrophobic and superhydrophobic, were performed to observe the evolutions of contact angle, contact radius and volume of the evaporating droplet. The evaporation dynamics of the squeezed droplet can be demarcated into two phases by a critical time t_p when the droplet pinches off from the upper surface. The CCR, CCA and the mixed evaporation mode of the squeezed droplet are observed before the pinch-off time t_p. However, the evaporation mode after t_p is highly dependent on the surface wettability and surface gap. Furthermore, the increased total evaporation time for the squeezed droplet in the narrower surface gap indicates that the squeezed droplet in a more confined space could significantly suppress its evaporation. To explain the inhibited evaporation of a squeezed droplet between two parallel surfaces, an ellipsoidal segment model is derived based on the isothermal diffusion-driven assumption, which could successfully predict the evolution of the droplet volume and contact radius during the CCA mode with high precision. Based on this model, the decrease of the evaporation coefficient λ for a narrower surface gap h suggests that the enrichment of vapor concentration near the droplet in the confined space is the origin of the mitigated evaporation of the squeezed droplet. Moreover, the unveiled linear scaling law between droplet volume and time, which is also reported in the studies of Portuguez [43], is explained by the cylindrical model simplified from the ellipsoidal segment model.

The evaporation of a liquid droplet with deformed morphology in a confined space is a common phenomenon in our daily life. For example, the drying of trapped or condensed liquid inside compact electronic products can be employed to mitigate or avoid water damage [66]. This type of droplet evaporation process also needs to be considered in various applications with a confined geometry including the microfluidic systems [44], fuel cells [45] and electrowetting-based actuation systems [44,46]. Our study about evaporation of squeezed water droplets between two parallel hydrophobic/superhydrophobic surfaces could deepen our understanding of droplet behaviors in these compact and complicated environments. The ellipsoidal segment model and the ideally simplified cylindrical model provide us with a versatile tool to predict and delineate the evaporation kinetics of squeezed droplets in a confined space. Furthermore, the insights presented in this work indicates that the enriched vapor concentration in the confined space is the primary reason inhibiting droplet evaporation, which offers us a guideline for manipulating droplets in a more complex environment.

6. Notice

This manuscript has been authored by UT-Battelle, LLC, under Contract No. DE-AC0500OR22725 with the U.S. Department of Energy. The United States Government retains and the publisher, by accepting the article for publication, acknowledges that the United States Government retains a non-exclusive, paid-up, irrevocable, world-wide license to publish or reproduce the published form of this manuscript, or allow others to do so, for the United States Government purposes.

CRediT authorship contribution statement

J.C. and X.H. conceived the research. J.C. raised the funding. X.H. conducted experiments and formal analysis. X.H., C.C. and B.S. fabricated the devices. D.B. developed black silicon nanofiber recipe. X.H. and J.C. wrote the manuscript. C.C. edited the manuscript.

Declaration of Competing Interest

None.

Acknowledgement

This work is financially supported by NSF CBET under grant number 1550299 and NSF ECCS under grant number 1808931. The fabrication of the black silicon nanofibers was conducted at the Center for Nanophase Materials Sciences of Oak Ridge National Laboratory, which is a DOE Office of Science User Facility.

Appendix A. Supplementary material

Supplementary data to this article can be found online at https://doi.org/10.1016/j.jcis.2020.05.003.

References

[1] P. Calvert, Inkjet printing for materials and devices, Chem. Mater. 13 (10) (2001) 3299–3305.
[2] J. Park, J. Moon, Control of colloidal particle deposit patterns within picoliter droplets ejected by ink-jet printing, Langmuir 22 (8) (2006) 3506–3513.
[3] G.T. Carroll, D. Wang, N.J. Turro, J.T. Koberstein, Photochemical micropatterning of carbohydrates on a surface, Langmuir 22 (6) (2006) 2899–2905.
[4] J.-Y. Jung, H.-Y. Kwak, Separation of microparticles and biological cells inside an evaporating droplet using dielectrophoresis, Anal. Chem. 79 (13) (2007) 5087–5092.
[5] T.-S. Wong, T.-H. Chen, X. Shen, C.-M. Ho, Nanochromatography driven by the coffee ring effect, Anal. Chem. 83 (6) (2011) 1871–1873.
[6] W. Jia, H.-H. Qiu, Experimental investigation of droplet dynamics and heat transfer in spray cooling, Exp. Therm. Fluid. Sci 27 (7) (2003) 829–838.
[7] J.T. Cheng, C.L. Chen, Active thermal management of on-chip hot spots using EWOD-driven droplet microfluidics, Exp. Fluids 49 (6) (2010) 1349–1357.
[8] J.T. Cheng, C.L. Chen, Adaptive chip cooling using electrowetting on coplanar control electrodes, Nanosc. Microsc. Therm. 14 (2) (2010) 63–74.
[9] A. Wu, L. Yu, Z. Li, H. Yang, E. Wang, Atomic force microscope investigation of large-circle DNA molecules, Anal. Biochem. 325 (2) (2004) 293–300.
[10] J. Jing, J. Reed, J. Huang, X. Hu, V. Clarke, J. Edington, D. Housman, T.S. Anantharaman, E.J. Huff, B. Mishra, Automated high resolution optical mapping using arrayed, fluid-fixed DNA molecules, Proc. Natl. Acad. Sci. U. S. A. 95 (14) (1998) 8046–8051.
[11] L. Zhao, J.T. Cheng, Analyzing the molecular kinetics of water spreading on hydrophobic surfaces via molecular dynamics simulation, Sci. Rep. 7 (1) (2017) 10880.
[12] L. Zhao, J.T. Cheng, The mechanism and universal scaling law of the contact line friction for the Cassie-state droplets on nanostructured ultrahydrophobic surfaces, Nanoscale 10 (14) (2018) 6426–6436.
[13] R.G. Picknett, R. Bexon, Evaporation of Sessile or Pendant Drops in Still Air, J. Colloid Interface Sci. 61 (2) (1977) 336–350.
[14] C. Bourgesmonnier, M.E.R. Shanahan, Influence of Evaporation on Contact-Angle, Langmuir 11 (7) (1995) 2820–2829.
[15] S.M. Rowan, M.I. Newton, G. Mchale, Evaporation of Microdroplets and the Wetting of Solid-Surfaces, J. Phys. Chem. 99 (35) (1995) 13268–13271.
[16] H.Y. Erbil, R.A. Meric, Evaporation of sessile drops on polymer surfaces: Ellipsoidal cap geometry, J. Phys. Chem. B 101 (35) (1997) 6867–6873.
[17] R.A. Meric, H.Y. Erbil, Evaporation of sessile drops on solid surfaces: Pseudospherical cap geometry, Langmuir 14 (7) (1998) 1915–1920.
[18] G. McHale, S.M. Rowan, M.I. Newton, M.K. Banerjee, Evaporation and the wetting of a low-energy solid surface, J. Phys. Chem. B 102 (11) (1998) 1964–1967.
[19] H.Y. Erbil, G. McHale, M.I. Newton, Drop evaporation on solid surfaces: Constant contact angle mode, Langmuir 18 (7) (2002) 2636–2641.
[20] Y.S. Yu, Z.Q. Wang, Y.P. Zhao, Experimental and theoretical investigations of evaporation of sessile water droplet on hydrophobic surfaces, J. Colloid Interface Sci. 365 (1) (2012) 254–259.
[21] G. McHale, S. Aqil, N.J. Shirtcliffe, M.I. Newton, H.Y. Erbil, Analysis of droplet evaporation on a superhydrophobic surface, Langmuir 21 (24) (2005) 11053–11060.
[22] F.C. Wang, H.A. Wu, Pinning and depinning mechanism of the contact line during evaporation of nano-droplets sessile on textured surfaces, Soft Matter 9 (24) (2013) 5703–5709.
[23] S.M.M. Ramos, J.F. Dias, B. Canut, Drop evaporation on superhydrophobic PTFE surfaces driven by contact line dynamics, J. Colloid Interface Sci. 440 (2015) 133–139.
[24] J. Lee, S.H. Hwang, S.S. Yoon, D.Y. Khang, Evaporation characteristics of water droplets in Cassie, Wenzel, and mixed states on superhydrophobic pillared Si surface, Colloids Surf. A 562 (2019) 304–309.
[25] W.D. Ristenpart, P.G. Kim, C. Domingues, J. Wan, H.A. Stone, Influence of Substrate Conductivity on Circulation Reversal in Evaporating Drops, Phys. Rev. Lett. 99 (23) (2007), https://doi.org/10.1103/PhysRevLett.99.234502.
[26] B. Sobac, D. Brutin, Thermal effects of the substrate on water droplet evaporation, Phys. Rev. E 86 (2) (2012) 021602.
[27] M.C. Lopes, E. Bonaccurso, Evaporation control of sessile water drops by soft viscoelastic surfaces, Soft Matter 8 (30) (2012) 7875–7881.
[28] S. Cioulachtjian, S. Launay, S. Boddaert, M. Lallemand, Experimental investigation of water drop evaporation under moist air or saturated vapour conditions, Int. J. Therm. Sci. 49 (6) (2010) 859–866.
[29] L. Bansal, S. Chakraborty, S. Basu, Confinement-induced alterations in the evaporation dynamics of sessile droplets, Soft Matter 13 (5) (2017) 969–977.
[30] L. Bansal, S. Hatte, S. Basu, S. Chakraborty, Universal evaporation dynamics of a confined sessile droplet, Appl. Phys. Lett. 111 (10) (2017) 101601.
[31] S. Hatte, R. Dhar, L. Bansal, S. Chakraborty, S. Basu, On the lifetime of evaporating confined sessile droplets, Colloids Surf. A 560 (2019) 78–83.
[32] J.R. Christy, Y. Hamamoto, K. Sefiane, Flow transition within an evaporating binary mixture sessile drop, Phys. Rev. Lett. 106 (20) (2011) 205701.
[33] G. Karapetsas, K.C. Sahu, O.K. Matar, Evaporation of Sessile Droplets Laden with Particles and Insoluble Surfactants, Langmuir 32 (27) (2016) 6871–6881.
[34] F. Clement, J. Leng, Evaporation of liquids and solutions in confined geometry, Langmuir 20 (16) (2004) 6538–6541.
[35] J. Leng, Drying of a colloidal suspension in confined geometry, Phys. Rev. E 82 (2) (2010) 021405.
[36] L. Daubersies, J.B. Salmon, Evaporation of solutions and colloidal dispersions in confined droplets, Phys. Rev. E 84 (3) (2011) 031406.
[37] S.J. Lee, J. Hong, Y.S. Choi, Evaporation-induced flows inside a confined droplet of diluted saline solution, Langmuir 30 (26) (2014) 7710–7715.
[38] C. Loussert, A. Bouchaudy, J.B. Salmon, Drying dynamics of a charged colloidal dispersion in a confined drop, Phys Rev Fluids 1 (8) (2016) 084201.
[39] R. Mondal, M.G. Basavaraj, Patterning of colloids into spirals via confined drying, Soft Matter 16 (15) (2020) 3753–3761.
[40] N. Maeda, J.N. Israelachvili, M.M. Kohonen, Evaporation and instabilities of microscopic capillary bridges, Proc. Natl. Acad. Sci. USA 100 (3) (2003) 803–808.
[41] E. Portuguez, A. Alzina, P. Michaud, A. Smith, Evaporation Kinetics and Breaking of a Thin Water Liquid Bridge between Two Plates of Silicon Wafer, Adv. Mater. Phy. Chem. 6 (07) (2016) 157–166.
[42] T. Soori, T. Ward, Evaporation and instability of an unbounded-axisymmetric liquid bridge between chemically similar and different substrates, J. Colloid Interface Sci. 539 (2019) 45–53.
[43] E. Portuguez, A. Alzina, P. Michaud, D. Hourlier, A. Smith, Study of the Contact and the Evaporation Kinetics of a Thin Water Liquid Bridge between Two Hydrophobic Plates, Adv. Mater. Phy. Chem. 7 (04) (2017) 99–122.
[44] S.Y. Teh, R. Lin, L.H. Hung, A.P. Lee, Droplet microfluidics, Lab Chip 8 (2) (2008) 198–220.
[45] J.G. Carton, V. Lawlor, A.G. Olabi, C. Hochenauer, G. Zauner, Water droplet accumulation and motion in PEM (Proton Exchange Membrane) fuel cell mini-channels, Energy 39 (1) (2012) 63–73.
[46] M.G. Pollack, A.D. Shenderov, R.B. Fair, Electrowetting-based actuation of droplets for integrated microfluidics, Lab Chip 2 (2) (2002) 96–101.
[47] X.G. Liu, P.R. Coxon, M. Peters, B. Hoex, J.M. Cole, D.J. Fray, Black silicon: fabrication methods, properties and solar energy applications, Energy Environ. Sci. 7 (10) (2014) 3223–3263.
[48] M. Badv, I.H. Jaffer, J.I. Weitz, T.F. Didar, An omniphobic lubricant-infused coating produced by chemical vapor deposition of hydrophobic organosilanes attenuates clotting on catheter surfaces, Sci. Rep. 7 (1) (2017) 11639.
[49] N.A. Fuchs, Evaporation and droplet growth in gaseous media, Pergamon Press, London, 1959.
[50] H. Hu, R.G. Larson, Evaporation of a sessile droplet on a substrate, J. Phys. Chem. B 106 (6) (2002) 1334–1344.
[51] H.Y. Erbil, Evaporation of pure liquid sessile and spherical suspended drops: A review, Adv. Colloid Interface Sci. 170 (1) (2012) 67–86.
[52] J.M. Stauber, S.K. Wilson, B.R. Duffy, K. Sefiane, Evaporation of Droplets on Strongly Hydrophobic Substrates, Langmuir 31 (12) (2015) 3653–3660.
[53] B. Qian, M. Loureiro, D.A. Gagnon, A. Tripathi, K.S. Breuer, Micron-Scale Droplet Deposition on a Hydrophobic Surface Using a Retreating Syringe, Phys. Rev. Lett. 102 (16) (2009) 164502.
[54] B.A. Qian, K.S. Breuer, The motion, stability and breakup of a stretching liquid bridge with a receding contact line, J. Fluid Mech. 666 (2011) 554–572.
[55] A. Akbari, R.J. Hill, Liquid-bridge stability and breakup on surfaces with contact-angle hysteresis, Soft Matter 12 (32) (2016) 6868–6882.
[56] H.B. Eral, D.J.C.M. 't Mannetje, J.M. Oh, Contact angle hysteresis: a review of fundamentals and applications, Colloid Polym. Sci. 291 (2) (2013) 247–260.
[57] H.Y. Erbil, G. McHale, S.M. Rowan, M.I. Newton, Determination of the Receding Contact Angle of Sessile Drops on Polymer Surfaces by Evaporation, Langmuir 15 (21) (1999) 7378–7385.
[58] P. Tsai, R.G. Lammertink, M. Wessling, D. Lohse, Evaporation-triggered wetting transition for water droplets upon hydrophobic microstructures, Phys. Rev. Lett. 104 (11) (2010) 116102.
[59] P. Papadopoulos, L. Mammen, X. Deng, D. Vollmer, H.J. Butt, How superhydrophobicity breaks down, Proc. Natl. Acad. Sci. USA 110 (9) (2013) 3254–3258.
[60] C. Antonini, J.B. Lee, T. Maitra, S. Irvine, D. Derome, M.K. Tiwari, J. Carmeliet, D. Poulikakos, Unraveling wetting transition through surface textures with X-rays: Liquid meniscus penetration phenomena, Sci. Rep. 4 (2014) 4055.
[61] H. Hu, R.G. Larson, Analysis of the microfluid flow in an evaporating sessile droplet, Langmuir 21 (9) (2005) 3963–3971.
[62] M.R. Barmi, C.D. Meinhart, Convective Flows in Evaporating Sessile Droplets, J. Phys. Chem. B 118 (9) (2014) 2414–2421.
[63] D.R. Lide, CRC Handbook of Chemistry and Physics: A Ready-Reference Book of Chemical and Physical Data (Book), 2004.
[64] M.J. Moran, H.N. Shapiro, D.D. Boettner, M.B. Bailey, Fundamentals of engineering thermodynamics, John Wiley & Sons, 2010.
[65] D.S. Golovko, H.-J.r. Butt, E. Bonaccurso, Transition in the evaporation kinetics of water microdrops on hydrophilic surfaces, Langmuir 25 (1) (2008) 75–78.
[66] A. Fukam, K. Nishimura, Forensic Analysis of Water Damaged Mobile Devices, Digit Invest 29 (2019) S71–S79.